THESIS

INTERNAL DOSIMETRIC EVALUATION OF CU-64-ATSM IN CANINE CANCER BEARING PATIENTS

Submitted by

Justin James Bell

Department of Environmental and Radiological Health Sciences

In partial fulfillment of the requirements

For the Degree of Master of Science

Colorado State University

Fort Collins, Colorado

Fall 2015

Master's Committee:

Advisor: Alexander Brandl

Brian Jones
Del Leary

ABSTRACT

INTERNAL DOSIMETRIC EVALUATION OF CU-64-ATSM IN CANINE CANCER BEARING PATIENTS

The assessment of the novel radiopharmaceutical Copper-64 diacetyl-bis(N4-methylthiosemicarbazones) (^{64}Cu-ATSMs) ability to selectively accumulate in hypoxic tumor tissue has been subject to ongoing research effort at Colorado State Universitie's (CSU) Veterinary Teaching Hospital (VTH). Due to the unique decay scheme of ^{64}Cu and internal distribution when bound to ATSM, the radiopharmaceutical has clinical importance as a possible Positron Emission Tomography/Computed Tomography (PET/CT) imaging agent with cancer theranostic potential. In this study, the PET/CT images of two cancer bearing canine patients treated with ^{64}Cu-ATSM were used to create patient specific voxelized phantoms that were compatible with the Monte Carlo N Particle extended (MCNPX) radiation transport code which was emplyed to retrospectively assess the internal radiation dose each patient received. By defining specific regions of interest (ROI) within the models, the dose to major organs was estimated. The derived models were designed as to dynamically approximate the relative dose each patient would receive to their tumor and normal tissue if the administered activity of ^{64}Cu-ATSM was altered. From these results, it was identified that the patient's malignances received ^{64}Cu-ATSM uptake at least during the acquisition of the patients' images. Organs such as the liver also had relatively high amounts of ^{64}Cu-ATSM uptake and were used to project what ROI might be dose limiting.

ACKNOWLEDGMENTS

I would like to thank all those on my committee for their support and willingness to aid in this research and the development of my Thesis. Your support, lessons, and guidance has helped me to grow as a research scientist, and has instilled a passion to continue my research pursuits.

Having mostly a radiation biology background with minimal experience and understanding of internal dosimetry, Dr. Brandl was brave as to take me on as his student. His openness, optimistic outlook, and helpful demeanor were an essential motivating factor for me to overcome the many research difficulties encountered. I am truly thankful for his support along with the support I received from those in the health physics section of the department.

Completing this project both directly and indirectly involved numerous people. I would like to thank Dr. Kato for first introducing me to the ongoing Cu-ATSM project, and for the invaluable research experiences he provided me. Many thanks to Dr. Mann for his help in establishing the internal dosimetry project, and for integrating me into the veterinary hospital. Thanks to Dr. Kraft for first allowing me to become involved with the ongoing Cu-ATSM research project and for her initial involvement on my committee. Thank you to Dr. Leary for being flexible and serving on my committee last minute. Thank you to Kevin Kirsch for aiding with all of the technical support at the veterinary hospital. To those involved in additional aspects of this work including; Christy, Jim, Ronda and Joe of the Radiation Control Office, Liz, and Chris Schmit at the veterinary hospital, and Kevin Capello, thank you all for your help. Funding for my education from the Nuclear Regulatory Commission has been greatly appreciated.

TABLE OF CONTENTS

Introduction

This research is motivated by the need to retrospectively assess the internal dose distribution that canine patients received while undergoing Positron Emission Tomography coupled with Computed Tomography at the Veterinary Teaching Hospital at Colorado State University. During these studies, the novel radiopharmaceutical Copper-64 diacetyl-bis(N4-methylthiosemicarbazone) (^{64}Cu-ATSM) was administered to patients in an ongoing study to evaluate the radiopharmaceutical's ability toward cancer imaging applications, to calculate the dose deposited through all forms of radiation, and possible therapeutic advantage. Thus, the patients' internal dosimetry will be modeled with Monte Carlo methodologies to identify dose-limiting organs at risk that might be detrimentally impacted through unnecessary toxicity if the administered dose is altered in future trials. Due to anatomical and malignant variance between patients, personalized voxel models were created specific to each patient and used in Monte Carlo N Particle extended (MCNPX) radiation transport code.

Internal Dosimetry

Radionuclides incorporated into the body via inhalation, ingestion, injection, or absorption can create unique challenges in determining an individual's radiation dose due to the dynamic and multivariable nature of the body. Internal dosimetry is the science of determining the spatial and temporal energy deposition of radiation to tissue from the decay of incorporated radionuclides. Due to the common inability to directly, and non-invasively measure specific regions of interest within the body, tools, methodologies, and models for performing internal dosimetry have been developed. Largely, the International Commission on Radiological Protection (ICRP) and the Committee on Medical Internal Radiation Dose (MIRD) have been responsible for fostering and refining many of the models and techniques used.

A successful model for calculating internal radiation dose needs to contain three main concepts; the physical radiation characteristics of the incorporated radionuclide, the organism's anatomy for which the dosimetry is being calculated, and the biokinetic behavior of the radionuclide or radiopharmaceutical. Model selection and application is therefore limited to model or phantom ability to best represent a specific individual with a defined incorporated radionuclide. Individual abnormalities that cause variations to one's spatial anatomy or have conditions that would alter the biokinetic behavior of an incorporated radionuclide would therefore deviate from a standardized model. Therefore, in select scenarios standardized models may not be representative of an individual, and would not as accurately estimate the internal radiation dose. Understanding the basic history of model development and methodologies aids in selecting a representative model or methodology to determine internal radiation dose.

Mathematical Models and Phantom Development

Many early approaches in estimating the dose of radiation from incorporated radionuclides were based on techniques and methodologies used for external radiation dosimetry. These dosimetric approaches were well validated for external radiation fields but did not directly correlate to the energy deposited from the decay of incorporated radionuclides. Typically when assessing external radiation fields, physical phantoms constructed of tissue-equivalent material with implanted radiation dosimeters were used to determine the absorbed dose. These phantoms are effective for external fields but are, "impractical to replicate the temporally-varying distribution of internal activities due to an unconfined radioactive source." (McParland, 2010) To account for basic temporal variances, initially mathematical models were developed and used to determine the internal radiation dose.

Mathematical Models

Marinelli and his colleagues in the 1940's derived some of the first formulations of internal dosimetry, taking into account activity and the basic mathematical representation of a radionuclide's retention time in an organ or tissue. (Martinelli & al., 1949) Though rudimentary, these equations identified two confounding factors in determining internal radiation dose related to the physical nature of the incorporated radionuclide and the biological retention of the radionuclide in the organism, setting the basic formalism for determining internal dosimetry. Expanding on Marinelli's calculations, researchers working along with the ICRP and MIRD committees further developed methodologies, often sharing commonalities between one another, as to better assess the dose from internal radiation. (Xu & Eckerman, 2009)

The ICRP, responsible for the development of recommendations and guidelines concerning radiation protection, released ICRP Publication 2, "Permissible Dose for Internal Radiation," in 1959. ICRP noted that, "The organs and tissues of the body exhibit varying degrees of radiosensitivity, and it is therefore necessary, for the purpose of protection, to consider their radiosensitvity with respect to specific functions as well as the dose they receive." (ICRP, 1959) Thus ICRP identified the need to assess individual regions of the human body when concerning internal dosimetry, and not solely the whole body dose. In 1975, ICRP 23 introduced Reference Man, which was designed to represent the anatomical and physiological characteristics of a population of people to more accurately estimate radiation dose. (ICRP, 1975)

ICRP Publication 2 was superseded in 1979 by ICRP Publication 30, "Limits for Intake of Radionuclides by Workers." (ICRP, 1979) ICRP Publication 30 introduced the concepts of committed dose and compartment models that mathematically divided the human body into

anatomical categories of organs and organ systems. Compartmentalizing the human body served as a means to model the biokinetic behavior or transfer of incorporated radionuclides between organs and organ systems. Understanding of the metabolism of radionuclides led to the development of the biological elimination constant used to determine the excretion rate of radionuclides. These models provided a better approximation for the activity per compartment as a function of time following the incorporation of radionuclides. (ICRP, 1979)

Stylized Phantoms

"The purpose of the phantom is to represent the organ or tissue of interest, to allow the radionuclide of interest to be contained in a specific volume, and provide a medium that absorbs and scatters the radiation emitted in a manner similar to tissue." (Zaidi & Sgouros, 2003) The development of stylized phantoms simplifies complex human anatomy into representative geometrical structures such as spheres, ellipsoids, and cylinders. Simplified geometries generalize the shape, location, and dimensions of specific organs in the body. Coupling these generalized anatomical models with Monte Carlo radiation transport computer codes provides the ability to determine the dose of radiation a specific organ may receive by radiation emitted from another location within the body.

MIRD is a subcommittee of the Society of Nuclear Medicine and Molecular Imaging responsible for, "Developing and improving a standardized framework and methodology for calculating internal radiation dose quantities in nuclear medicine." (SNMMI, 2015) Historically MIRD has been involved with the development of multiple anthropomorphic phantoms along with standardizing the methodology to calculate internal radiation dose form administered radiopharmaceuticals used in nuclear medicine. The MIRD models were designed to provide

dose estimates that would be used to determine biological endpoints, therefore differing from ICRP that was concerned with evaluating risk endpoints.

Phantoms developed by MIRD were coupled with Monte Carlo radiation transport code simulations to derive absorbed fractions. Stylized models such as the MIRD 5 phantom, developed according to the ICRP-23 approximations of Reference Man, more accurately represented major airways, abdominal cavities, and cranial structures of a typical human. (Snyder & al, 1978) The ALGAM Monte Carlo transport code, developed at ORNL, at the time was only capable of transporting photons, but further development of transport codes such as ETRAN, EGS4, and MCNP4A allowed for the transport of electrons and other modes of radiation thus improving and deriving new absorbed fractions. (Zaidi & Sgouros, 2003) Absorbed fractions, commonly designated as Φ, represent the average absorbed dose of radiation deposited in a defined target organ or region of interest by radiation emitted from a location within the body referred to as the source organ.

MIRD Formalism

The MIRD formalism was developed amid technological advances such as the application of advanced Monte Carlo radiation transport codes. The MIRD formalism generally subdivides an organism's body into sources of radiation and target regions, to assess if the radiation released from a defined source may impart energy into the defined target. Conveniently The location of activity within the body from which radiation would be emitted is identified as the source organ, r_S, and the target tissue for which dose is being calculated is identified as the target organ, r_T. As shown in the following equation, the mean dose of a target organ is calculated as a function of time. (McParland, 2010)

$$D(r_T, T_D) = \sum_{r_S} A(r_s, t) \frac{1}{M(r_T, t)} \sum_i E_i Y_i \Phi(r_T \leftarrow r_s\, E_i t)$$

Where $D(r_T, T_D)$ is the dose to a specific target organ, r_T, during an integrated time period T_D . The activity of each source organ, r_s, at time t is represented by $A(r_s, t)$, and the mass of the target organ at time t is denoted as $M(r_T, t)$. The mean energy emitted by a specific decay mode i is represented by E_i, with Y_i representing the yield of the specific radiation emission per nuclear transformation. The absorbed fraction, $\Phi(r_T \leftarrow r_s E_i t)$, is the energy imparted in the target organ by radiation originating from the source organ, following a specified nuclear transformation at time t. By utilizing standardized reference phantoms, MIRD calculates S-factors that replace the absorbed fraction to simplify the calculations as shown in the following equation. (Snyder, 1975)

$$D(r_T, T_D) = \sum_{r_S} A(r_s, t)\, S(r_T \leftarrow r_S)$$

S-factors libraries were created specific to each phantom and radionuclide combination. Various calculation tools and codes were created to aid in the calculation of internal radiation such as the MIRDOSE code that incorporated radionuclide libraries and derived absorbed fractions for multiple phantoms. Users enter the relative biokinetic behavior or residence times a radionuclide has in source organs, and the program calculates S-values to be used to calculate dose. As shown in the following equation, the basis of these programs simplified MIRD's initial equations to calculate dose, D_T, to a target organ relative to the number of disintegrations in a source tissue, N_S, with a derived dose factor, DF, that accounted for the absorbed radiation dose to the target organ per number of nuclear transformations in each source organ. (Bolch, 2002)

$$D_T = N_S \times DF$$

The MIRDOSE code has since been rewritten in Java language and renamed as Organ Level Internal Dose Assessment (OLINDA) providing the ability for the code to function on multiple computer platforms and assess both external and internal radiation dose. The Radiation Dose Assessment Resource (RADAR) provides electronic access to a multitude of resources

including decay data, absorbed fractions relative to multiple phantoms, dose factors, and kinetic data for over 800 radionuclides. (Bolch, 2002) RADAR is set up in a fashion as to allow open access to many of their recourses, and serve as a source of help and knowledge for assessing radiation dose. (The Radiation Dose Assessment Resource)

Tomographic or Voxel Phantoms

Voxelized or tomographic whole body phantoms have become more common with advancements in medical imaging and computational technologies used in modern medicine. Instead of applying stylized models that are based on geometrical approximations of average anatomical characteristics to derive absorbed fractions, voxelized models use an individual's CT or MRI images to produce an anatomically precise model that can be used with Monte Carlo radiation transport codes to determine absorbed fractions. This methodology aims to eliminate individual anatomical variances, and allows for further flexibility in designating regions of interest. (Zaidi & Sgouros, 2003)

CT scans function as to acquire continuous segmented axial image slices of a patient. Each slice contains a 256x256 or 512x512 matrix of picture elements per planar image, commonly referred to as pixels. Pixels can be multiplied by the CT slice thickness to obtain a representative volume or voxel. (Bushberg, Seibert, Leidholdt, & Boone, 2012) By stacking multiple CT slices 3-dimensional figure or model comprised of voxels can be created. Depending on the computational power and memory available, voxels can be classified as individual targets or sources of radiation following fundamentals of the MIRD formalism, therefore providing the ability to create a finely segment model that is highly representative of an individual.

An example of more generalized voxel models is the Virtual Human Project (VHP) managed by the US National Library of Medicine. The VHP utilizes CT and MRI images of

male and female cadavers to create 3-dimensional anatomically correct models. These models were used to create the VIP-Man that is 3-dimentinal anatomically correct human model containing around 3 billion voxels. The derived models more accurately represent the geometry of the human body to allow for accurate transport of radiation when incorporated with Monte Carlo radiation transport codes. (McParland, 2010) (Xu, Chao, & Bozukurt, VIP-MAN: An Image-Based Whole-Body Adult Male Model Constructed from Color Photographs of The Visable Human Project for Multi-Particle Monte Carlo Calculations, 2000)

Radioactive Decay

Neutrons, protons, and electrons are subatomic particles that comprise atoms. Protons and neutrons form the nucleus of an atom, and are comprised of three elementary particles referred to as quarks. Protons are made of two up quarks, each having a charge of +2/3 e, and one down quark, having a charge of -1/3 e, giving the proton an overall charge of +1 e. Neutrons are comprised of two down quarks and on up quark giving them an overall neutral charge. Electrons are an example of leptons and have $\frac{1}{2}$-integer spin with an overall charge of -1 e. (Cember & Johnson, 2009)

Modern physics considers four fundamental forces; the strong force, weak force, electromagnetic force, and gravitational force. The four forces dictate how radiation is emitted as well as how it interacts with matter and transfers energy. The strong force or color force is responsible for holding together quarks and binding protons and neutrons together in the nucleus. The weak force or weak nuclear force can change the flavor of quarks, providing the ability for protons and neutrons to be converted into one another. The electromagnetic force is the combination of the electric and magnetic forces that dictate charged particle interactions. The

gravitational force is used to explain the attractive force that objects with mass have on one another. (Bushberg, Seibert, Leidholdt, & Boone, 2012)

Elements are classified by atomic numbers or the number of protons contained within an atom's nucleus. Isotopes are atoms relative to each element but varying by atomic mass, reflecting that the atom has the same number of protons and electronic structure, but differs in the number of neutrons contained within the nucleus. The stability of the nucleus is determined by the ratio of neutrons and protons it contains. A narrow range in the neutron to proton ratio within the nucleus exists that allows for the formation of stable nuclei. Radioisotopes lie outside this region of stability due to increases or decreases to their neutron to proton ratio. (Cember & Johnson, 2009)

Acting within the nucleus, the Coulomb force and the strong force combat one another to break apart or hold together the nucleus of an atom. The Coulomb force is part of the electromagnetic force in that charged particles will repel one another with a force proportional to the product of their like charges and inversely proportional to their proximity. Therefore, positively charged protons within the nucleus repel one another. Counteracting this repulsive Coulomb force is the strong nuclear force; acting over a very limited distance it binds neutrons and protons together. At low atomic numbers, stable nuclei often have the same number of protons and neutrons. As the number of protons increases within the nucleus, eventually additional neutrons, exceeding the equal number of protons, needs to be present in the nucleus as to counteract the columbic repulsion. (Cember & Johnson, 2009)

Radioactivity

Unstable or excited nuclei may undergo nuclear transformations to achieve nuclear stability. In doing so, the energy that is conserved in the binding energy of the nucleus is released

as kinetic energy or the emission of radiation, likewise the relaxation or transition of a nucleus from a higher energy state to a lower energy state will cause the release of energy as radiation. The mode of nuclear transformation or decay is dictated by characteristics of the atom and the energy available during the nuclear transition. The available energy depends on the nature of the unstable atom and the mass energy relationship between the parent nucleus and the daughter nucleus. (Cember & Johnson, 2009) Incorporating these physical principles of decay, unstable atoms may undergo alpha emission, isobaric transitions, and isomeric transitions to achieve a stable state nucleus.

Alpha emission is one example of particle emission. Alpha particles consist of a helium nucleus, or two protons and two neutrons, therefore having an atomic mass of 4 u and a charge of 2+ e. Typically, heavier atoms with a low neutron to proton ratio and an atomic number greater than 82 may undergo alpha emission. Following the emission of an alpha particle, the daughter nucleus will have an atomic mass deficit of four and an atomic number that is two less than the parent. This can be seen in the following equation with X representing the parent nuclide, Y representing the daughter nuclide, with A and Z representing the atomic mass and the atomic number respectfully. (Cember & Johnson, 2009)

$$^{A}_{Z}X \rightarrow {}^{4}_{2}He + {}^{A-4}_{Z-2}Y$$

Isobaric Transitions

Isobaric transitions produce daughter products that have the same atomic mass number as the parent nuclei, but will vary in the number of neutrons and protons contained in the nucleus. The atomic number will vary based on the specific decay mechanism that the parent nucleus undergoes to transition from an excited state to a stable state. Beta minus emission, positron

emission, and electron capture are all examples of isobaric decay mechanisms. (Turner, 2008) (Cember & Johnson, 2009)

An unstable atom with a high neutron to proton ratio may transition to a stable state by the emission of a beta minus particle, β^-, coupled with an anti-neutrino, $\bar{\nu}$. The emission of a beta minus particle and anti-neutrino occurs due to the weak force allowing a neutron in the nucleus of the atom to convert into a proton. The energy available from this nuclear transition is not solely transferred to the beta particle, but also to the anti- neutrino, therefore the emission of a beta particle will exhibit a continuous energy distribution as a portion of the energy will be shared with the anti-neutrino. (Cember & Johnson, 2009) (Turner, 2008)

$$^{A}_{Z}X \rightarrow {}_{Z+1}{}^{A}Y + \beta^- + \bar{\nu}$$

Positron emission, or beta plus emission, occurs in nuclei with low neutron to proton ratios, when the emission of an alpha particle is not energetically favorable. Inversely to beta minus emission, a proton within the nucleus of an atom will transform into a neutron, emitting a positron, β^+, and an neutrino, ν. Positrons are the antiparticle of the electron, having the same mass as the electron but proportionally positively charged. Similar to beta minus emission, the available energy from the nuclear transition will be shared between the positron and the neutrino, therefore emitted positrons will display a continuous energy distribution. Unlike beta emission, positron emission will only occur if the mass of the unstable parent nucleus exceeds the mass of the daughter nucleus by two electron masses. (Cember & Johnson, 2009)

$$^{A}_{Z}X \rightarrow {}_{Z-1}{}^{A}Y + \beta^+ + \nu$$

Orbital electron capture will occur when an unstable nucleus has a low neutron to proton ratio, but the mass difference between the unstable parent and the daughter is less than the mass of two electrons, preventing positron emission from occurring. (Cember & Johnson, 2009)

During electron capture, an orbital electron is absorbed by the nucleus of the unstable parent to transform a proton within the nucleus to a neutron. The atomic mass of the nucleus will be the same but the atomic number of the daughter nucleus will be one less than the parent. In the process, a neutrino is emitted.

$$ {}^{A}_{Z}X + e^{-} \rightarrow {}_{Z-1}{}^{A}Y + \nu $$

Isomeric Transitions

Isomeric transitions reduce the nuclear energy state of an atom and produce a nucleus with the same atomic mass and atomic number as the parent. Gamma ray emission and internal conversion are the two main isomeric transition mechanisms unstable nuclei undergo. (Cember & Johnson, 2009) (Turner, 2008)

Gamma rays are a form of electromagnetic radiation released from the nucleus of the atom, characteristically having a high frequency and no mass. Typically, the emission of a gamma ray is preceded by another form of nuclear decay such as the emission of an alpha or beta particle that leaves the daughter nucleus in a metastable or excited state. As the nucleus transitions from an exited state to a lower energy state, the energy difference between the initial and final energy states will be released through the emission of a gamma ray. (Cember & Johnson, 2009)

During internal conversion, an excited nucleus interacts with an orbital electron, transferring the nucleus' excess energy to the electron causing it to be ejected from the atom. Higher energy orbital electrons will fill the vacancy in the electron orbital resulting from the ejected electron. As higher energy electrons fill inner orbital vacancies, characteristic X-rays will be released with the discrete energy of the difference between the two orbital states between which the electron transitions.

The energy released during the electron transition from a higher energy state to a lower energy state could also cause the emission of Auger electrons. During Auger emission, the energy difference between the orbital states will be converted into kinetic energy of an orbital electron, thereby ejecting the electron from the atom as an Auger electron. This mechanism produces an additional electron orbital vacancy that can be filled in the same manner, thus causing additional electrons to be ejected, often referred to as an Auger cascade. (Turner, 2008) Auger electrons have relatively low energies, allowing Auger electrons to strongly interact with the surrounding medium and deposited a high amount of energy per average distance traveled in the medium.

Activity

Activity describes the temporal rate of nuclear transformations, measured in units of Becquerels (Bq) or Curies (Ci). A Becquerel describes a single decay or disintegration per second, (Turner, 2008) compared to a Ci that describes the activity of a sample relative to 1g of ^{226}Ra. The activity of a pure radionuclide sample decreases exponentially with time as shown by the following equation, where A is the activity at time t from an original activity of A_0.

$$A = A_0 e^{-\lambda t}$$

The radionuclide decay constant, λ, describes how the fraction of activity will decrease with time. Another means to represent the time kinetics involved in the decay of radionuclides is the radionuclide half-life, or time it takes for the activity of an original sample to be reduced by one half. The radionuclide decay constant and half-life, T, are related through the following equation.

$$T = \frac{ln(2)}{\lambda}$$

Interactions of Radiation with Matter

In a medical setting it is especially important to understand how radiation interacts with matter to take advantage of specific mechanisms that can aid in treatment and imaging, while avoiding detrimental effects to patients. The mechanisms in which radiation interacts and deposits energy into matter are largely dependent on the composition of the target and the type and energy of the incident radiation. Radiation interacts and transfers energy through excitation and ionization of the atoms comprising the target material. During excitation, energy transferred from radiation to orbital electrons does not exceed the electron's binding energy, and will cause the electron to move to a higher energy state. Ionizations occur when the energy transferred from incident radiation to the absorbing atom exceeds the binding energy of the orbital electron, causing the electron to be ejected from the atom to form an ion pair. (Cember & Johnson, 2009)

Photon interactions

Photons are uncharged, massless electromagnetic radiation that carry energy proportional to their frequency. Photons are sparsely ionizing and will either be absorbed, scattered, or do not interact when passing through material. X-rays and gamma rays are both examples of photons, and are indistinguishable from one another except for the location of their production in that gamma rays are produced intranuclear and x-rays are produced extranuclear. Photons interact with matter through four main mechanisms; Rayleigh scattering, the photoelectric effect, Compton scattering, and pair production, with a probability dictated by the energy of the incident photon and the composition of the target material. (Bushberg, Seibert, Leidholdt, & Boone, 2012)

At very low energies, photons will exhibit Rayleigh scattering. Rayleigh scattering is a parametric process in that the incident low energy photon will not alter the quantum state of the

target atom following interaction. The low energy photon will instead excite the entire atom causing the atom's electrons to oscillate in phase. (Bushberg, Seibert, Leidholdt, & Boone, 2012) The atom's electron cloud will release the imparted energy as a photon of the same energy as the incident photon, but will alter the photon's direction. This mechanism corresponds to elastic scattering of the low energy photon.

The photoelectric effect ensues when an incident photon has the same or marginally more energy than the binding energy of an orbital electron in a target atom. As shown by the following equation, an incident photon with energy E_p is absorbed by a target atom's orbital electron, causing the ejection of the electron from the valence shell as the energy from the incident photon is transferred to the electron. The ejected electron is referred to as a photoelectron and will have an energy, E_{pe}, equal to the difference between the energy of the incident photon and the binding energy, E_{be}, of the orbital electron.

$$E_{pe} = E_p - E_{be}$$

The photoelectric effect is most prominent when photons interact with materials comprised of high atomic numbers. Small changes in the material composition such as increases to the atomic number have a profound effect on the probability of the photoelectric effect occurring. This has importance in medical radiology because bone contains large amounts of calcium that has a relatively larger atomic number as compared to the elements that comprise soft tissue. Therefore, the absorption of photons by the photoelectric effect is amplified in bones as compared to soft tissue, providing the basic contrast desired for radiographs.

Orbital vacancies caused by the ejection of an orbital electron will be filled by other valence electrons with higher potential energy. The transition of a higher orbital electron to fill a lower energy orbital vacancy will cause the release of energy manifested as a characteristic x-ray

photon with energy proportional to the energy difference between the transitioned orbital energy states. It is possible for a non-optical, direct energy transfer to a valence shell electron to occur, causing the electron to be ejected from the atom as an Auger electron. The emission of an Auger electron therefore perpetuates the atoms orbital vacancy. The probability of characteristic x-ray emission versus the emission of an Auger electron depends on the atomic number of the target atom. High Z elements have a higher probability of producing characteristic x-rays than emitting Auger electrons following the ejection of an orbital electron. (Cember & Johnson, 2009) (Turner, 2008)

Compton scattering takes place when an incident photon with energy much larger than the binding energy of an orbital electron, collides with an orbital electron in an elastic collision causing the electron to be ejected from the atom and the incident photon to be scattered. The probability of Compton scattering increases with higher energy photons, and with increased electron densities of the target medium. Most elements per unit mass have a comparable number of electrons; therefore the Compton Effect is independent of the atomic number of the material but related to the density of the material. (Cember & Johnson, 2009) (Turner, 2008)

Pair production occurs when incident photons have energies exceeding 1.02 MeV. During this mechanism, the kinetic energy of the incident photon will be converted into mass, typically in the proximity of an atom's nucleus, producing a particle and antiparticle pair such as an electron and a positron. The energy of the incident photon must exceed the rest mass energy of the particle pair for this mechanism to take place. Diagnostic imaging uses photons at energies lower than what would allow for pair production to take place, but in some modalities of radiation therapy, pair production may occur. (Bushberg, Seibert, Leidholdt, & Boone, 2012)

Particle Interactions

Unlike Photons, charged particles such as alpha and beta particles interact with the surrounding environment by electrostatic forces that cause the particles to continuously loose energy while exciting orbital elections of the surrounding medium. Similar to photons, particle radiation has a probability of colliding with an atom's nucleus itself as a means of transferring energy.

Beta minus particles that are emitted from the nucleus of an atom, have a -1 e charge with a mass equal to that of an electron, and can undergo rapid changes in velocity, or direction, when traveling proximal to an atom's nucleus. (Cember & Johnson, 2009) This change in velocity is caused by the attractive Coulomb force the positively charged nucleus has on the negatively charged beta particle. Inversely, a positron with a +1 e charge will be repulsed by the like charged nucleus of an atom causing it to change its velocity. The change in the particle's velocity results in Bremsstrahlung photons with a continuous energy distribution related to the incident particle's change in energy. The probability of Bremsstrahlung to occur increases with the Z of the material an electron is traversing. (Cember & Johnson, 2009)

Positrons or beta plus particles will exhibit similar interactions with matter such as bremsstrahlung during flight. Positrons are composed of antimatter, and at low energies will interact with a surrounding electron resulting in the annihilation of both the positron and the electron and the emission of two 511 keV photons 180° opposite of one another. Positron Emission Tomography relies on this interaction of anti-matter and matter to produce photons for detection.

Heavier charged particles, such as the alpha particle, have a higher mass and charge than beta particles. Alpha particles and other heavy charged particle radiation exhibit straighter flight

paths through target material due to the particle's increase in mass. At high energies, the charged particle's electric field has a weakened ability to interact with the electron's in the target material, resulting in less kinetic energy transfer from the particle to the target material. As the particle slows down in a material, the ability for the particle's electric field to interact with surrounding electrons increases, providing the ability to transfer energy at a higher rate, causing a local increase of excitations and ionizations in the target material. (Cember & Johnson, 2009) (Turner, 2008) (Bushberg, Seibert, Leidholdt, & Boone, 2012)

Linear energy transfer (LET) is a term that describes the average energy imparted from a radiation particle per unit distance. The general classification of high and low LET is used to categorize different types of radiation at specific energies. While charged particles lose energy and slow down, increased interactions between the charged particle and surrounding material will occur. Increased interactions with the surrounding material allow for an increase of energy deposition for the charged particle, therefore increasing the LET. Generally for charged particle radiation, the LET per nucleon will increase as the particle's charge and mass increase, while the energy of the particle decreases. Photons lack charge and mass, and do not continuously interact with matter. Secondary particles produced by photons are categorized as low LET radiation. Important to this research, Auger electrons are classified as higher LET radiation since the Auger electron will deposit larger amounts of energy to the target medium over shorter distances because of the Auger electron's low initial energy.

Monte Carlo Radiation Transport Codes

Monte Carlo is a mathematical methodology that can be used to derive a numerical solution of a non-probabilistic problem by using probabilistic methods of repeated random number sampling. Almost all Monte Carlo codes used presently incorporate the Monte Carlo

mathematical process alongside a defined simulation that is used to model the progression of a desired process. The model describes the key characteristics and behaviors that are naturally displayed within a system, but allows for the user to alter or influence conditions within a set parameter of the system to better understand the implications each condition has on the mean outcome.

Radiation interactions with matter are probabilistic in nature, influenced by both the incident radiation and the material it is traversing. This stochastic process makes it impossible to predict specifically how a single particle of radiation will interact with matter, but with a sufficient number of independent evaluations, coupled with a finite variance, an expected value or mean can be determined through the application of the central limit theorem. (Kalos & Whitlock, 2008) Monte Carlo radiation transport codes have the ability to simulate the transport of individual radiation particles, sequentially assessing the probabilistic events of each particle's interaction within the transport process, and report aspects of the simulated particle's mean behavior. Statistically sampling the probability distributions that dictate particle interactions provides the mean behavior of the system, assuming a large enough sample size is used.

Imaging Modalities

Imaging modalities and their application in medicine vary due to differences in their acquisition technologies and the types of energies they require. Imaging variances provide each modality with relative strengths and limitations based on the desired application objectives. Combining imaging modalities serves to complement limitations and shortcomings of one modality with strengths of another. Positron Emission Tomography (PET) coupled with Computed Tomography (CT) has become a useful combined imaging modality in oncology, cardiology, and neurology due to its ability to align anatomical information derived from CT

images with functional information from PET images. Specifically PET/CT has become a regular diagnostic tool used for cancer detection, staging, and ongoing treatment assessment. (Beyer, et al., 2000)

Computed Tomography

CT scans have a central role in modern medical imaging due to the detailed anatomical and morphological information they can provide. Similar to traditional radiography, CT images are produced by detecting the passage of x-rays through a patient. An x-ray tube is located on one side of the patient and produces a known distribution of x-rays directed towards the patient. The x-ray photons directed at the patient will be attenuated, scattered, absorbed, or will not interact as they pass through the patient's body. The attenuation, scattering, and absorption of the incident x-rays will alter the distribution of x-ray energies exiting the patient's body that are collimated and detected by an array of solid-state scintillation detectors. (Bushberg, Seibert, Leidholdt, & Boone, 2012)

The Gantry design of the CT system allows for the x-ray tube and the adjacent detector array to be rotated around the patient. Rotating the system around the patient's body provides the ability to image the patient at a large number of angles. Computer algorithms are used to process the radiation transmission data collected by the detectors into a tomographic image. The tomographic image represents a section or "slice" of the patient's body spatially spanning x and y components. Human patients are typically imaged in a supine position on a patient table or "couch", while many animal patients are imaged based on the limitations of the patient and the objectives of the scan. The patient couch serves to position the individual within the bore of the scanner, and move the patient during the image acquisition. The patient's cranial caudal axis is positioned parallel to the z-axis of the scanner allowing the patient can be moved along the z-axis

and reimaged to produce multiple transvers image slices. The consecutive tomographic images or slices are computationally aligned producing a 3-dimensional image of the patient. (Bushberg, Seibert, Leidholdt, & Boone, 2012)

Anatomic information provided by CT imaging relies on changes in the tissue structure that can be used to identify, size, stage, and to some extent the metastasis of a tumor. X-ray CT scanners most commonly use a tube voltage of 120 kV, (Bushberg, Seibert, Leidholdt, & Boone, 2012) but the tube voltage can be altered to provide an optimized image quality with the tradeoff of increasing the patient's dose. X-ray transmission from a monoenergetic beam follows the principles described by the following equation:

$$I = I_0 e^{-\sum_{i=1}^{n} -\mu_i x_i}$$

where I_0 represents the original intensity of the x-rays produced by the x-ray tube, μ_i represents the attenuation coefficient relative to each tissue type, and x_i represents the material thickness. By utilizing a multitude of beam and detector angles, the relative attenuation coefficients can be derived for specific areas within the patient and are assigned a corresponding Hounsfield unit. Hounsfield units are used to standardize the determined attenuation coefficients shown in the following equation relative to a scale from -1000 corresponding to air to +1000 corresponding to bone.

$$CT - Value = Hounsfield\ Unit(HU) = 1000\left(\frac{\mu - \mu_{water}}{\mu_{water}}\right)$$

Assigning grey scale levels to each derived Hounsfield unit allows for the production of the final grey scale image that provides contrast for CT images. (Boellaard, et al., 2010)

Positron Emission Tomography

PET imaging provides functional information based on the distribution and localization of radiopharmaceuticals within a patient's body. PET scanners are designed to detect the two 511

keV annihilation photons produced by the annihilation of a positron, emitted by the nuclear transformation of an administered radionuclide. Specifically, Annihilation Coincidence Detection (ACD) is used in PET detectors to determine the distribution of an administered radionuclide within a patient. (Bushberg, Seibert, Leidholdt, & Boone, 2012) The acquired PET images can be fused with CT images to provide both anatomical and physiological information about the patient. (Gambhir, 2002)

PET detectors are comprised of scintillation crystals attached to photomultiplier tubes arranged in a ring formation around the patient. Similar to CT scans, PET scans will acquire images of the patient in axial image slices. If the annihilation photons are emitted in a detectable orientation, and are not scatted during flight, the photons will interact with the detector ring opposite one another at slightly different times, relative to the distance traveled by the photon to the detector. The detector is designed to detect the incident photons and create a pulse signal describing the location of interaction, and the time of interaction to discriminate if detected interactions are characteristic of annihilation photons. If the detected photons pass the discriminator, the relative difference of the photon's time from annihilation to detection is used to project back where the annihilation of the positron occurred. (Bushberg, Seibert, Leidholdt, & Boone, 2012)

The PET image is reconstructed and corrected to account for limitations of the detector such as dead time, and coincidence. The difference in time it takes for the annihilation photons to interact with the detectors allows for the location of the annihilation to be estimated within a few centimeters. (Bushberg, Seibert, Leidholdt, & Boone, 2012) Factors such as the angle of the annihilation photons, distance required for the annihilation photons to travel before detection,

patient movement, and intrinsic spatial resolution impact and limit the overall resolution of the PET scan.

Radiopharmaceuticals

The application of radiopharmaceuticals coupled with radiation detectors has provided the unique ability to internally map patient's physiological functions in a non-invasive manner. As applied in nuclear medicine, radiopharmaceuticals can be used to trace, diagnose, and treat various diseases. As the name implies, radiopharmaceuticals consist of a radioactive tracer molecule or radionuclide bound to a pharmaceutical component or carrier molecule. Combinations of carrier molecules and radionuclides are selected based on the desired application. (Gambhir, 2002) (Strauss & DimitrakopoulouStrauss, 2008)

Radionuclide Selection

The selection of radionuclides used in specific radiopharmaceuticals is complex and often multivariable taking into account the desired application, safety, convenience, and cost. The physical characteristics of the radionuclide selected for use in a radiopharmaceutical often dictates its application as a diagnostic or therapeutic agent, but also is the root cause of the associated safety concerns. From a radiological protection and safety standpoint there is no "ideal" radiopharmaceutical because all radiopharmaceuticals have the potential to contribute radiation dose to the patient, supporting nuclear medicine staff, or other bystanders. Therefore, theorized ideal radiopharmaceuticals utilize radionuclides that minimize radiation exposures to all personal involved while still providing the desired medical outcome. (Bushberg, Seibert, Leidholdt, & Boone, 2012)

Ideal physical characteristics of radionuclides used in diagnostic imaging are; relatively short lived, exhibit limited particle emissions, and provide an abundance of photons with a

desired energy. The half-life of the radionuclide is important as to be long enough for the exam to be completed, but short enough to allow for fast image acquisition and minimization of a patient's dose. Additionally, the half-life needs to be taken into consideration if transport and modification of the radionuclide is required. With the exception of positrons, nuclear transitions that result in the emission of charged particles typically do not provide diagnostic advantages and only contribute to patient dose. Similarly, lower energy photons have a higher probability of being attenuated within the patient, contributing to the patient's dose without improving the quality of the image. Increasing the photon energy increases the likelihood of the photon to leave the patient's body, but at too high of energies decreases the photon detection efficiency. Currently, most of the scintillation detectors used in medicine are optimized for photon energies around 140 keV. (Bushberg, Seibert, Leidholdt, & Boone, 2012)

Radiation therapies' objective is to deposit radiation dose to target tissues while minimizing the dose of radiation to non-targeted tissues. The desired physical characteristics of radionuclides used in therapeutic radiopharmaceuticals therefore differs from that used in diagnostic imaging, but still takes safety implications, convenience, and cost into consideration.

Carrier molecules

Radionuclides will naturally distribute throughout the body and concentrate in tissues based on the size and charge of the radionuclide. The distribution of a radionuclide within the body be can be altered by binding a carrier molecule to the radionuclide. The binding of a carrier molecule to alter the biokinetic behavior of a radionuclide within the body is the basis of radiopharmaceuticals. Ideally, the carrier molecule used in radiopharmaceuticals should be designed to concentrate to targeted tissues or regions of interest while minimizing uptake to non-

targeted tissue, to improve the contrast of the image and minimize radiation dose to non-target tissues.

The most commonly used radiopharmaceutical for PET/CT imaging of tumors is ^{18}F-Fludeoxyglucose (FDG). FDG is a glucose analog recognized and processed by cells as glucose, thus FDG is selective for areas of high glycolytic activities, which are often found in tumor tissues. Flourine-18 is the radionuclide used in FDG, and because it predominantly emits positrons it will deposit relatively low amounts of energy in the patient. (Hess, Blomberg, Zhu, Høilund-Carlsen, & Alavi, 2014)

Production

The radionuclides used in radiopharmaceuticals are not naturally present or at least present in abundance due to their short half-lives; therefore, the radionuclides used in nuclear medicine are artificially created. Nuclide generators, nuclear reactors, and particle accelerators can be used in nuclear medicine to generate the desired radionuclides. (Bushberg, Seibert, Leidholdt, & Boone, 2012)

Accelerators can accelerate charged particles to high energies and direct them into stable target nuclei with the use of a cascading series of transformers. The high energy of the charged particle allows the particle to overcome the Coulomb barrier, which normally would repulse positive ions, to interact with the target atom's nucleus resulting in the production of a radionuclide. The resulting products are typically proton rich with a high specific activity, but come with a relatively high cost. (Bushberg, Seibert, Leidholdt, & Boone, 2012)

Cyclotrons are modified linear accelerators that consist of a vacuum chamber containing two closely positioned semicircular electrodes, within the poles of an electromagnet. A high alternating voltage is applied between the two electrodes so that when ions, typically protons,

deuterons, alpha particles, and negatively charged hydrogen ions, are injected into the center of the system, they are accelerated towards the electrode that is oppositely charged. Reversing the polarity between the electrodes causes the particle to accelerate, while the magnetic field created by the electromagnet restrains the particles from leaving the system by retaining it in a circular path. Particles gain kinetic energy as the radius of the particles' path increases. Particles that reach the desired kinetic energy are removed from the system by a charged deflector plate, and directed towards the target material. The accelerated particles collide and transfer energy to the nuclei of the target atoms, resulting in the production of radionuclides. The radionuclides produced by cyclotrons tend to have a high proton to neutron ratio in the nucleus; therefore, the radionuclides will typically undergo positron emission or electron capture decay. (Bushberg, Seibert, Leidholdt, & Boone, 2012) (Cember & Johnson, 2009) (Turner, 2008)

Nuclear reactors differ utilize neutrons to excite the nucleus of target atoms. Neutrons do not carry charge; therefore, the neutron will not be affected by the Coulomb repulsion of the target atoms, negating the need to accelerate them to high energies. Radionuclides used in radiopharmaceuticals can be produced either from fission products of the nuclear reactor or by using the nuclear reactor to neutron activate a target material. The application of either method results in a neutron rich product.

In a fission reaction, the nucleus of an atom is in a highly unstable state and undergoes fission, or the splitting of the atom's nucleus, producing fission products. Fission yields provide the probability of yielding specific fission products. The radionuclides that are used in radiopharmaceuticals require chemical separation from the other fission products. (Bushberg, Seibert, Leidholdt, & Boone, 2012)

Nuclear activation also takes advantage of the neutrons produced in a nuclear reactor to activate target material that can be used for radiopharmaceuticals in nuclear medicine. Most commonly, thermal neutrons present in the reactor will collide with a positioned sample of source material, causing the nuclei of the target material to capture the neutron, resulting in a radionuclide that typically decays by beta-minus emission. Neutron activation reactions typically involve the capturing of a thermal neutron followed by the release of a gamma-ray, but less commonly an alpha particle or a proton can be released. The main difference in using neutron activation to produce radionuclides is that the resulting activated target material will have a low specific activity because carrier molecules that were not activated will be present, along with any impurities that existed in the initial target. (Bushberg, Seibert, Leidholdt, & Boone, 2012)

Radionuclide generators function differently than particle accelerators and nuclear reactors because they are designed to exploit the natural decay of the radionuclides. The parent radionuclide of a desired daughter is housed in the radionuclide generator, and as the parent decays into its daughter product the radionuclide generator allows for the separation from the parent material. Radionuclide generators are commonly used in nuclear medicine when the desired daughter product does not have a sufficiently long half-life to be transported from the site of production to the desired site of application. Therefore, the system is limited to its application based on the relationship between the desired daughter product and the decay of the parent nuclide. This system provides a product with high specific activity at a relatively low cost. (Bushberg, Seibert, Leidholdt, & Boone, 2012)

Copper-64

^{64}Cu can be produced through three main mechanisms that vary in the level of specific activity and yield of the product. Producing ^{64}Cu by thermal neutrons via the ^{63}Cu (n, γ) ^{64}Cu

reaction will produce a product with low specific activity and low yield. High energy neutrons can be used to produce ^{64}Cu by the ^{64}Zn (n, p) ^{64}Cu reaction with a higher specific activity but low yield. The biomedical cyclotron is most commonly used to produce ^{64}Cu for medical applications by the ^{64}Ni (p, n) ^{64}Cu reaction the results in a product with high specific activity and high yield. (Eckerman, Westfall, Ryman, & Cristy, 1994)

^{64}Cu is a relatively short-lived radionuclide with a half-life of 12.701 hours, and decays either ^{64}Zn by internal conversion, or to stable ^{64}Ni by electron capture (EC). Undergoing EC will leave the atom as a whole in an excited state, due to the vacancy left from the absorbed inner electron; therefore, the atom will transition into a ground state by either the emission of characteristic x-rays or by the release of Auger electrons.

The relative yields of each form of radiation emitted from ^{64}Cu were taken from the National Nuclear Data Center (NNDC) from Brookhaven National Laboratory (BNL) sponsored by the United States Department of Energy (DOE) and organized into Table1. (NNDC, 2015)

Table 1: Decay yield and energies of ^{64}Cu

Nuclear Transition	NT % Yield		Decay mode	Energy (keV)	Intensity (%)
Internal Conversion	38.5		Beta Minus	190.7	38.5
Electron Capture	61.5	17.6	Positron	278.21	17.6
		43.9	Gamma-ray & X-ray	0.85	0.489
				7.461	4.74
				7.478	9.3
				8.265	1.12
				8.265	0.58
				1345.77	0.475
				Sum	16.704
			Auger	0.84	57.5
				6.54	22.51
				Sum	80.01

ATSM

The ligand carrier Diacetyl-bis(N4-methylthiosemicarbazone) (ATSM) has unique properties that can be useful in a clinical setting do to its preferential localization to hypoxic tissue. (Maurer, et al., 2002) ATSM has high membrane permeability but a low redox potential providing the ability to be incorporated into cells, but will not be reduced by the cell's mitochondria. (Fujibayashi, et al., 1997) Rather, Cu is hypothesized to be reduced in hypoxic environments where disassociation from the carrier ATSM is also thought to take place. (Dearling, Lewis, Mullen, Welch, & Blower, 2002) The reduction of Cu and its dissociation from ATSM can occur in normoxic tissue, but it is hypothesized that re-chelation takes place at a higher rate than in hypoxic environments, therefore ideally causing the accumulation of Cu in hypoxic tissues rather than normoxic tissues.

Biological Implications

Radiation has two main mechanism with which it will interact with deoxyribonucleic acid (DNA), known as the direct and indirect effect. By the indirect effect, incident radiation will interact typically with water molecules that surround the DNA, causing the radiolysis of the water molecules and the formation of reactive oxygen species (ROS). ROS produced proximal to DNA can cause oxidative stress that damages the DNA. The indirect effect occurs predominantly from exposures to low LET radiation. (Hall, 2012) The direct effect is proposed to be the main mechanism that high LET radiation interacts with DNA. During the direct effect, incident radiation either reacts directly with the DNA itself or with molecules surrounding the DNA, but instead causes the ejection of electrons from the surrounding molecules that will directly interact with, and damage the DNA.

Tumor Microenvironment & Hypoxia

A multitude of factors that differentiate cancerous growths from normal tissues have been identified as potential targets for diagnostics, prognostics, and therapy applications. Tissue oxygen concentrations have historically affected the prognosis of tumors hindering the ability to successfully utilize typical radiation therapy techniques and chemotherapeutic agents. (McMillan, 2015) Identifying and characterizing hypoxic regions within tumors has clinical benefit for more accurate prognosis, staging, and treatment design.

Areas of abnormally low oxygen concentration within the body are termed hypoxic. Tissues intrinsically vary in oxygen concentration; therefore hypoxia measured relative to the designated tissue. In normal subcutaneous tissue the partial pressure of oxygen (pO_2) is approximately 50 mmHg, whereas hypoxic tissues may have a pO_2 less than 10mmHG. (Carreau, El Hafny-Rahbi, Matejuk, Grillon, & Kieda, 2011) Hypoxic conditions occur during tumor development and in some instances can display a self-promoting process. Failure to degrade factors such as Hypoxia-inducible factor (HIF-1) in cancer cells allows for unregulated transcription of genes associated with angiogenesis, erythropoiesis, and glycolysis. Angiogenic signals released from the cell will promote the ingrowth of new vasculature, but as seen in tumors the new vasculature to be sporadic and locally disorganized. The irregular vasculature growth in tumors has been known to mix arterial and venal blood, causing a reduction in the amount of available oxygen within the blood vessels. The decreased availability of oxygen is coupled with oxygen's ability to only diffuse about 0.2mm from the vessel to cause a decrease of available oxygen in tumor tissues. The hypoxic condition further promotes the transcription and activation of factors associated with angiogenesis such as the vasculature endothelial growth factor (VEGF) and other factors. (Hall, 2012) (Weinberg, 2007)

Tumors with hypoxic conditions are known to be resistant to common photon radiotherapy. The oxygen enhancement ratio relates the differences of radiation dose needed to achieve the same biological effect with varying oxygen concentrations. (Hall, 2012) Hypoxic cells and tumors tend to be more radioresistant than normaoxic cells and tumors. The hypothesized underlying mechanism is that oxygen will bind to sites of DNA damage such as DNA double strand or single strand breaks, causing what is referred to as, "oxygen fixation." Oxygen to the broken ends of the DNA inhibits proper DNA repair to take place. (Bertout, Patel, & Simon, 2008) Radiation therapy is designed as to increase the radiation dose to targeted tumor tissue to create more DNA damage that will ideally result in the death of the targeted cells. Therefore, the decreased ability to repair DNA as described in oxygenated conditions would be beneficial in targeting tumor cells, but hypoxic conditions would allow for radioresistance.

Traditional photon therapy has been found to be less effective in the treatment of hypoxic tumors. Interestingly, the cell killing associated with exposures to high LET radiation is not reliant on the concentration of oxygen in the local tissue environment, meaning hypoxic and normoxic cells display the same sensitivity to high LET radiation exposures. ^{64}Cu-ATSM having the ability to locate to regions of hypoxia, as well as emit low penetrating, high-LET Auger electrons could have therapeutic advantages in the treatment of hypoxic tumors. This notion is supported by the publication, "Validation of ^{64}Cu-ATSM damaging DNA via high-LET Auger electron emission," in which hypoxic cells treated with ^{64}Cu-ATSM died due to exposures from high-LET Auger electrons produced by the decay of ^{64}Cu, incorporated into cells by its bound carrier molecule ATSM. (McMillan, 2015)

Materials & Methods

^{64}Cu-ATSM Radiolabeling

The Cyclotron Research Group that is part of the Department of Medical Physics at the University of Wisconsin-Madison produced the ^{64}Cu that was used in this study. Using the published methodology (Avila-Rodriguez, Nye, & Nickles, 2007), a 11.4 MeV cyclotron bombarded a ^{64}Ni enriched target forming ^{64}Cu through a ^{64}Ni(p, n) ^{64}Cu reaction. The resulting ^{64}Cu was suspended in a 0.1M HCl solution and shipped via FedEx to CSU Central Receiving, but was formally received at the nuclear medicine laboratory at the CSU VTH Flint Animal Cancer Center.

The activity of the ^{64}Cu solution was evaluated with an Atomlab 500 dose calibrator (Biodex, Shirly, NY). The volume was evaluated by comparing the mass difference between a tare vial and the solution vial with an assumed liquid density of 1 g/ml. An equal volume of a 4:1:5 solution of 1M Glycine, 1M NaOH, and Deionized H_2O was added to the ^{64}Cu solution vial. A volume of 1mM ATSM was added equal to that of the original ^{64}Cu solution plus the 4:1:5 solution. Finally, a volume of 2% Na-Ascorbate equal to the total contents of the solution vial containing the ^{64}Cu solution, 4:1:5 solution, and the 1mM ATSM, was added and allowed to rest for 20 minutes. ATSM used in the trials was synthesized as reported (Gingras, Suprunchuk, & Bayley, 1961) and supplied by Dr. Furukawa from the National Institute of Radiological Sciences (NIRS) located in Chiba, Japan. (Fujibayashi, et al., 1997)

Thin lay chromatography (TLC) was used to determine the efficiency of the radiolabeling by adding a small volume of the prepared ^{64}Cu-ATSM solution to the bottom of a TLC, before partially submerging a small portion of the TLC plate in an organic carrier such as ethyl acetate. Successfully labeled ^{64}Cu-ATSM would migrate with the mobile phase, while unbound ^{64}Cu

would remain in the stationary phase. The TLC plate was separated into a bottom quarter and a top three-quarters, before being evaluated by the dose calibrator. Following successful chelation of ^{64}Cu-ATSM, the desired activity to be administered to the patient was separated from the ^{64}Cu-ATSM solutions and mixed into a saline solution. (McMillian, 2013)

Image Acquisition

For the purpose of this research, two canine patients, referred to as Patient 1 and Patient 2 were used to derive voxel models. Patient 1 was a 12-year-old mixed bread female canine with a mass of 42 kg, that had a large left thoracic wall mass diagnosed by biopsy as myxosarcoma. The patient was sedated, and positioned similarly as seen in Figure 1, prior to a whole body and post-contrast CT scan being performed. 5.57 mCi of ^{64}Cu-ATSM was administered to the patient preceding a whole body PET acquisition by 60 minutes. Patient 2 was a 7-year-old, 34 kg female yellow Labrador Retriever with a right humeral osteosarcoma. A similar image acquisition as recorded for Patient 1 was applied to Patient 2 with an administered activity of 4.71 mCi ^{64}Cu-ATSM. From the PET/CT acquisition, an additional soft tissue mass was located in the caudal aspect of the nasopharynx and thought to be a possible polyp.

Figure 1: Canine Patient being positioned before the initiation of the image acquisition

Software Packages

The protocol for voxelization of the patients CT images followed previously reported methodologies utilizing Voxelizer software. (Martinez, Johnson, Capello, & Pinder, 2014) (Ruedig, Beresford, Gomez Fernandez, & Higley, 2015) (Caffrey, 2013) This methodology was chosen due to the availability of necessary software and local experience and support.

Intellispace

The Philips Intellispace Portal by Koninklijke Philips Electronics was used to initially analyze the acquired PET/CT images at the Veterinary Teaching Hospital. The Intellispace Portal is a useful clinical tool allowing physicians the ability to store, organize, and share patient records as well as it allows users to view a multitude of image modalities derived from various images systems that can produce a DICOM standard file type. DICOM files have become the standardized medical imaging format by the Medical Imaging and Technology Alliance as to allow for the circulation and examination of medical images. (Philips Clinical Informatics , 2015)

A multitude of clinical based viewing functions are available with the software, allowing for CT and PET acquisitions to be fused together as shown in Figure 2 and Figure 3. Specific organs were defined and traced with the use of region of interest tools. The defined regions of interest could be manually traced to quantitatively analyze the ROI's volume and activity. The patient's DICOM file could then be exported onto an external memory device to be used to create the voxel model. (Philips Clinical Informatics , 2015)

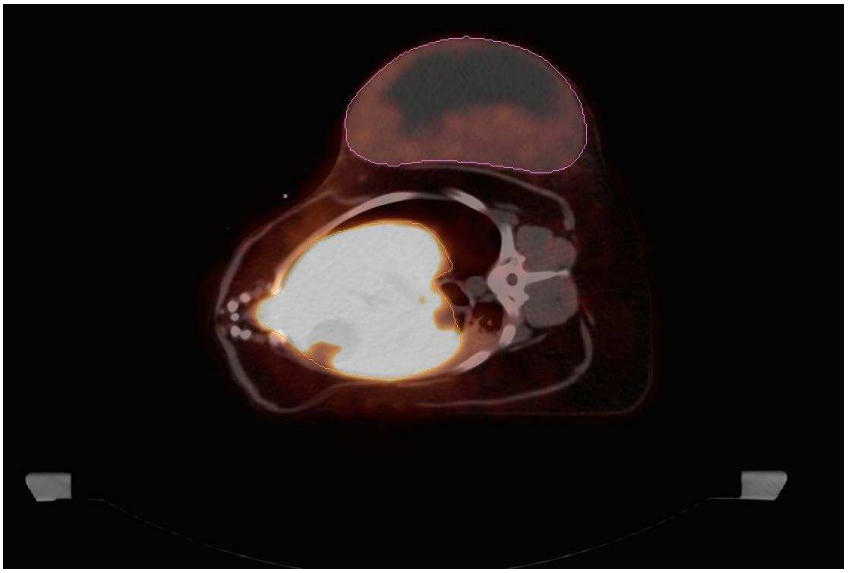

Figure 2: Fused PET/CT image of Patient 1 as seen with the Intellispace Software.

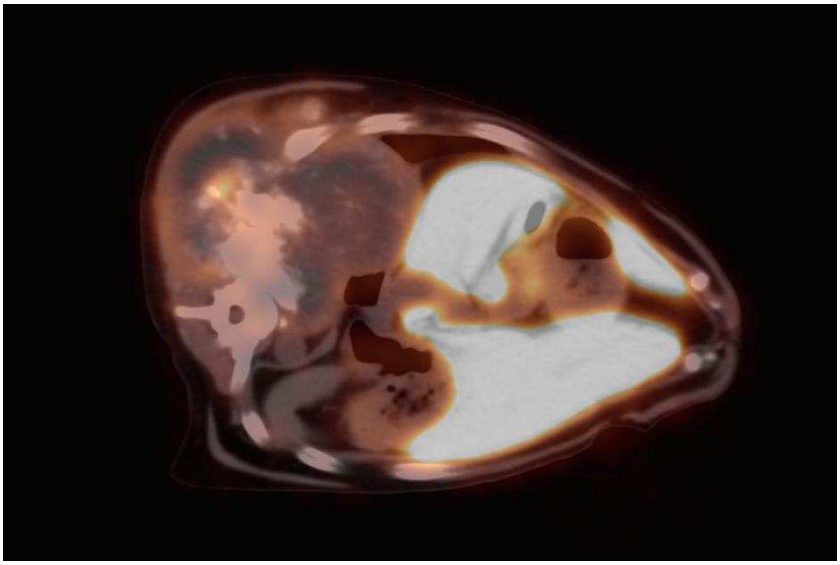

Figure 3: Fused PET/CT image of Patient 2 as seen with the Intellispace Software.

Specifically, the Intellispace software was used to derive the volumes of defined ROI, as well as it supplied the number of counts within a region of interest. The volumes of the ROI were compared to the volumes derived from the 3D-Doctor software, to quantify variations between the software measurements and user induced variations. The number of counts measured within each ROI were used to determine the percent distribution of the administered ^{64}Cu-ATSM in the patient's body. The derived percent distribution was incorporated into the final dose evaluation equations. Each of the patient's original 5 mm, 512x512 CT images were used to derive the patient specific models with 3D-Doctor, and the acquired whole body CTAC NLHQ PET image was used to fuse with the patient's CT image to determine the percent uptake within each ROI.

3D-Doctor

3D-Doctor is an FDA approved medical imaging 3D visualization software produced by Able Software Corporation capable of handling MRI, CT, PET, and other cross-sectional image modalities. The software itself contains a multitude of image processing tools as well as segmentation options providing the user the ability to manually and automatically-segment images, shown in Figure 4, to allot 3D volume rendering and quantitative analysis. 3D-Doctor supports a large number of imaging file formats, and most importantly enables the user to export derived mesh models to a multitude of file formats for further external processing.

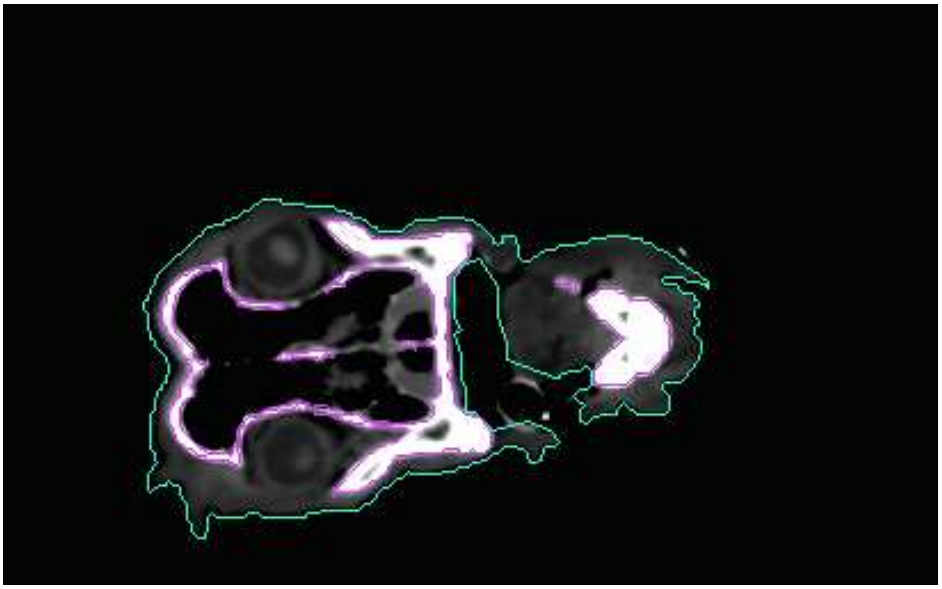

Figure 4: Example of patient cranial segmentation in 3D-Doctor

The exported DICOM files from the Intellispace software that contained the patient's CT acquisitions were imported into 3D-Doctor. 3D-Doctor provides the ability to create virtual phantoms from original DICOM image stacks by allowing the user to define boundaries or regions of interest (ROI's) within the patient's body. The software provides useful tools such as auto-segmentation processes that identify general anatomical boundaries that can be further shaped and manipulated with boundary editing tools. Predominantly, these tools did not always work as advertised, and required the boundaries to be manually defined with the use of a graphics tablet, in slice to slice increments. Once complete, the resulting boundaries generate a patient specific, anatomically correct, virtual phantom of the patient as shown in Figure 5 that can be exported as a boundary file (.bnd)

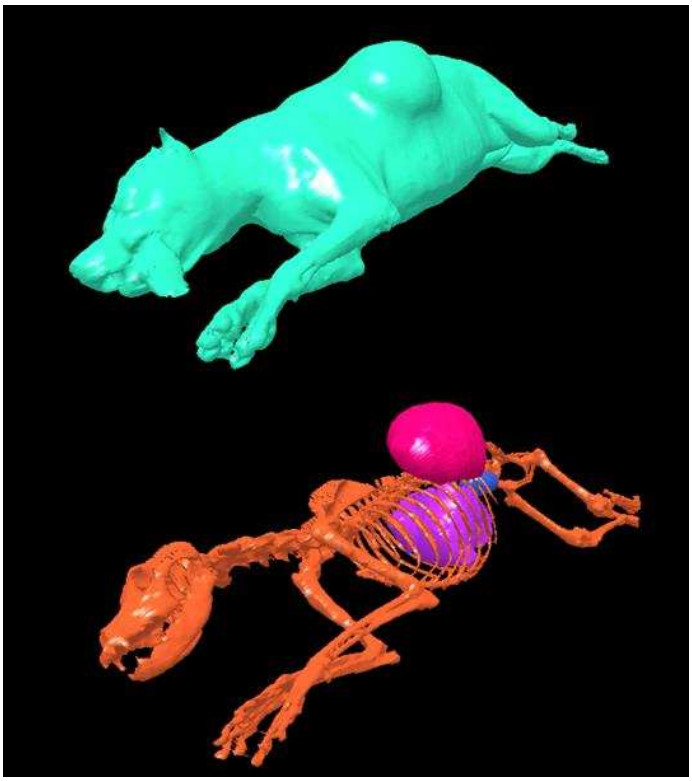

Figure 5: 3D model representation of Patient 1 in 3D-Doctor with and without remaining tissue.

The ability to export .BND files is essential to generate MCNPX lattice geometries with the use of lattice generating programs such as Voxelizer. Boundary line data files or .bnd are simple ASCII text files used to represent geometrical contours or boundaries. The syntax for exported .BND files is shown in Figure 6. The Z numbers refer to the slice number relative to the contoured image used in 3D-Doctor, and the X and Y values provide points of spatial information for each slice. Each contour or polygon is closed with the keyword "END," and the end of the file is designated with an "END END" (Able Software Corp, 2015)

Z_1
X_{1N}, Y_{1N}
END
Z_2
X_{2M}, Y_{2M}
END
END

Figure 6: example .BND file syntax

Voxelizer

Voxelizer, originally written in VisualBasic.NET, is a program developed by Kevin Capello and Erick Cardenas-Mendez of the Human Monitoring Laboratory of Canada that converts 3D-Doctor derived, boundary files into input geometries or lattice structures that are compatible with Monte Carlo N Particle (MCNPX) code input specifications. Additional to the 3D-Doctor boundary file, Voxelizer requires the input of CT acquisition parameters such as slice thicknesses, number of rows and columns, and pixel size. The acquired CT images of the canine patients were 5 mm slices with a 512 mm matrix, therefore providing a voxel width and height of 1.7188 mm. Voxelizer creates a temporary work file or a .vxl file while converting the virtual phantom defined in the boundary file into a MCNPX compatible lattice structure, shown in Figure 7. Additional tools such as the SDEF helper, also created by the Human Monitoring Laboratory, were used to define the volume source within the subsequent lattice structure.

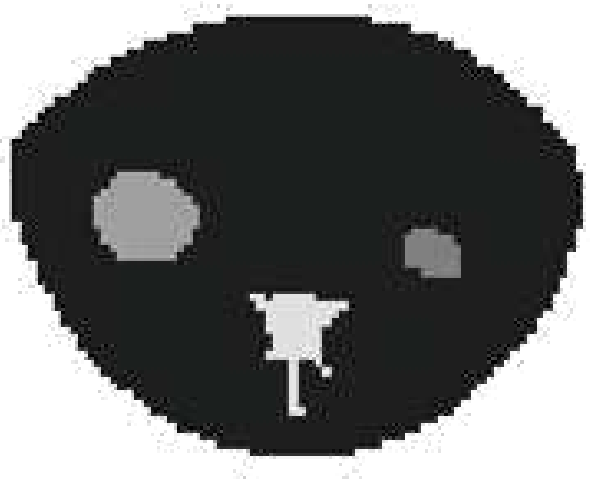

Figure 7: Example cross section of a derived voxel model as viewed with Voxelizer

The resulting MCNPX lattice structure produced by voxelizer is relatively large, but can be modified by using a built in compression function. Difficulties arose when applying this function. Typical errors occurred when the geometry was not well centered and a compression

factor was applied. Shown in Figure 8, this would cause the compressed geometry to wrap outside of the overall universe, rendering the phantom unusable. (Kramer G. H., 2010)

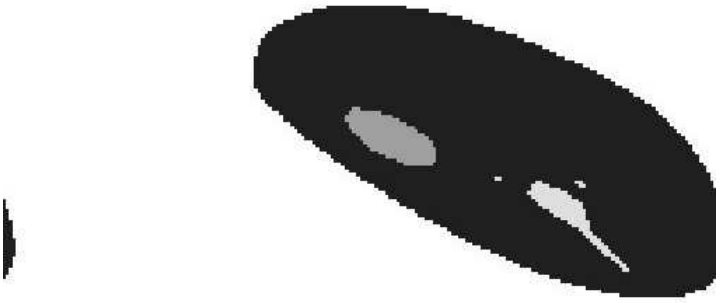

Figure 8: Example of warped geometry caused a compression factor of 2

MCNPX

Monte Carlo N-Particle extended (MCNPX) transport code is a radiation transport code developed by Los Alamos National Laboratory that allows for the radiation transport of particles at designated energies through user specified materials. The original code was developed in the late 1950's but has been continuously improved and revalidated. The code itself is written in FORTRAN-90 language, but only requires the user to provide a well-defined input file.

The user supplied input files are required to be written in a specific structure. The input file is divided into three main sections; Cell Cards, Surface Cards, Data Cards, that are all separated by a blank line delimiter. Cell and surface cards are used to create and define 3-dimensional geometries within the MCNPX simulation universe. The geometries used in this study were all in a lattice format produced by Voxelizer.

The material composition of the model followed the composition and density of soft tissue and bone defined by ICRP. (McConn, 2010) The SDEF card used to define the source of radiation was generated by the SDEF helper that utilized the MCNPX geometry to designate a specific universe in which the source would be defined. The monoenergetic forms of radiation

produced by the decay of ^{64}Cu were derived from that listed by the NNDC. (SITE) The beta energy spectrum used for both positrons and beta minus particles was supplied by RADAR. (The Radiation Dose Assessment Resource) The energy deposition tally, *F8, was used to measure the total energy deposition in MeV in select universe. 7000000 starting particles were used for each run.

MNCPX only allows one particle type to be run at a time. Therefore, separate runs were required with each particle type; Beta minus, Gamma, Auger, and Positron. Additionally, to derive specific dose fractions contributed to each target region by a single source region, each organ was run separately as a source with the other segmented regions designated as targets, therefore the dosimetric assessment of each patient included a total of 24 runs. The corresponding MCNPX output files supplied the energy imparted in each tally described in units of MeV.

Results

Voxelized models were created for two canine patients, referred to as Patient 1 and Patient 2. Patient CT images were segmented into ROI's that included; Brain, Tumor, Left Kidney, Right Kidney, Liver, Bone, and Remaining Tissue (RT). Remaining tissue was comprised of any tissue that was not individually segmented and therefore included much of the musculature system, respiratory tract, and gastrointestinal tract. The volumes of the derived ROI's from the Intellispace and 3D-Doctor software were compared. Their respective volumes differ by less than 10%. The derived volumes from 3D-Doctor along with the tissue densities from ICRP (McConn, 2010) were used to approximate the mass of each ROI as shown in Table 2.

Table 2: Mass and percent uptake for each patient's ROI

	Patient 1		Patient 2	
ROI	Mass (kg)	Uptake (%)	Mass (kg)	Uptake (%)
Brain	0.0740	0.315	0.0919	0.624
Liver	0.9190	37.657	0.8788	38.215
Left Kidney	0.0856	0.589	0.0566	0.953
Right Kidney	0.0943	0.568	0.0798	1.417
Tumor	1.6942	2.166	0.4706	1.491
RT	43.1962	58.704	35.9010	57.299

Patient's percent uptake in each ROI was determined with the Intellispace software that supplied the summation of the detected counts, or detected annihilation photon pairs, in each defined ROI. The derived percent distribution was used to approximate the static distribution of ^{64}Cu-ATSM within each patient's body.

From the MCNPX output files, the mean energy imparted in a target tissue per nuclear transition in a source tissue was determined in units of MeV. The radiation yield along with the relative ROI percent uptakes were factored into the derived energy contributions.

The energy contributions per starting particle were summed for each target ROI and converted from MeV to dose in Gray (Gy) by dividing by the mass of the relative ROI. The resulting absorbed fractions for Patient 1 and Patient 2 are shown in Table 3 and Table 4 with LK, RK, and RT, representing left kidney, right kidney, and remaining tissue respectively.

Table 3: Absorbed fractions for Patient 1 in Gy per decay of ^{64}Cu

Patient 1	Source						
Target	Brain	Liver	LK	RK	RT	Tumor	Total
Brain	2.57E-16	2.20E-18	1.22E-20	6.71E-21	8.67E-17	1.14E-19	3.46E-16
Liver	2.00E-20	3.42E-15	4.71E-18	2.59E-18	1.74E-16	4.20E-18	3.61E-15
LK	7.41E-21	3.19E-16	4.23E-16	7.35E-18	2.17E-16	2.42E-18	9.69E-16
RK	4.53E-21	1.76E-16	7.51E-18	3.75E-16	2.18E-16	5.43E-18	7.82E-16
RT	3.84E-19	9.29E-17	1.75E-18	1.71E-18	1.98E-16	2.55E-18	2.97E-16
Tumor	1.70E-20	6.95E-17	6.01E-19	1.32E-18	7.97E-17	1.25E-16	2.76E-16
Bone	1.22E-17	3.67E-16	5.09E-18	3.68E-18	5.71E-16	7.86E-18	9.67E-16
					Whole Body		7.24E-15

Table 4: Absorbed fractions for Patient 2 in Gy per decay of ^{64}Cu

Patient 2	Source						
Target	Brain	Liver	LK	RK	RT	Tumor	Total
Brain	3.77E-16	5.06E-19	4.77E-21	5.25E-21	8.01E-17	9.10E-19	4.59E-16
Liver	9.04E-21	3.11E-15	6.08E-18	2.94E-18	1.36E-16	3.92E-19	3.26E-15
LK	2.68E-21	2.47E-16	8.89E-16	5.93E-18	1.57E-16	1.06E-19	1.30E-15
RK	2.43E-21	1.61E-18	3.96E-18	9.76E-16	1.55E-16	7.18E-20	1.14E-15
RT	7.43E-19	7.85E-17	2.23E-18	3.31E-18	1.81E-16	2.13E-18	2.68E-16
Tumor	3.80E-19	9.73E-18	6.45E-20	6.36E-20	9.35E-17	2.17E-16	3.21E-16
Bone	1.30E-17	1.76E-16	3.96E-18	4.92E-18	3.76E-16	8.41E-18	5.82E-16
					Whole Body		7.32E-15

As depicted in Tables 4 and 5, each absorbed fraction can be scaled by the number of ^{64}Cu nuclides administered to the patient to estimate the radiation dose to each ROI and the whole body.

Discussion

By incorporating patient specific voxelized models into MNCPX, the average energy imparted in a target ROI per nuclear transition of ^{64}Cu-ATSM was derived. These results supply information required to calculate the internal radiation dose received by the patient from a known administered activity of ^{64}Cu-ATSM. Specifically, the radiation dose to each designated ROI can be determined. The results from this examination provides insight as to what ROI may be the dose-limiting factor if ^{64}Cu-ATSM was to be used as a therapeutic agent, thereby requiring an increase in the administered dose.

The creation of these models was intended to be patient specific, providing the dose estimates derived for the two patients relative to their individual anatomy and biologic interaction with ^{64}Cu-ATSM. These models can be used as a reference for determining the approximate dose expected in further trials, but it is crucial that they are not used as a working model for new patients to dictate alterations to the administered dose. Patients in this trial both bore different forms of cancer, therefore the internal distribution and behavior of ^{64}Cu-ATSM may have been altered based on characteristics of each malignancy. Anatomical variances existed between the two patients and their corresponding models that are apparent in the variance between the derived dose factors. Patient breed variance would have an impact on anatomical differences between the canines, but also alter the distribution of ^{64}Cu-ATSM.

The ROI selected for this study were preliminary, and to more accurately represent the patient's internal organization any future models should include other radiosensitive tissues or tissues with high uptake such as the lung and the intestine. By defining additional ROI, future models will provide more accurate approximations of local uptake, and provide a more accurate dose reconstruction.

The mass differed between the measured mass of each patient and the total mass of the calculated model. The model for Patient 1 had an excess mass of 4.06 kg, and the model of Patient 2 had an excess mass of 3.48 kg. The mass of each ROI was determined from its segmented volume. A mass variance could have occurred due to physical density variations in the patient that would be assumed homologous in the model. Additionally, the lungs and all other internal airways were not separately segmented form the models, and were instead incorporated into the model as remaining tissue and given the corresponding density of soft tissue. Both factors could account for the mass difference observed, but further efforts should be taken as to definitely determine the source of this variance.

The same beta energy spectrum was assumed for the simulated beta minus and positron MCNPX runs. It was hypothesized that positrons and beta minus particles would contribute about the same amount of dose to the patient, neglecting the dose contribution from the annihilation photons, and most if not all of the energy from the two particles would be deposited within the source organ. It was found that the positron and beta minus dose contribution derived from the results of the MCNPX runs did not match that of the average energy of the beta particle spectrum used in this study. The positron dose contribution was significantly higher as compared to the dose contribution of the beta minus particles. This is shown in Table 5 and Table 6.

Table 5: Mean Energy deposition from beta minus particles in units of MeV per starting particle for Patient 1

P1 Beta -	Source					
Target	Brain	Liver	LK	RK	RT	Tumor
Brain	0.038378	0	0	0	8.14E-21	0
liver	0	0.038384	4.20E-08	4.08E-09	4.32E-07	0
LK	0	1.45E-05	0.038379	7.77E-09	5.85E-08	0
RK	0	0	8.82E-09	0.03838	6.39E-08	1.45E-10
RT	2.21E-08	1.45E-05	1.95E-05	1.85E-05	0.038392	7.32E-06
Tumor	0	4.44E-09	0	6.23E-09	2.38E-07	0.038391
Bone	2.05E-05	2.58E-07	1.11E-07	3.81E-08	2.47E-06	3.34E-08

Table 6: Mean energy deposition from positrons in units of MeV per starting particle for Patient 1

P1 Beta +	Source					
Target	Brain	Liver	LK	RK	Skin	Tumor
Brain	0.1221	1.50E-05	5.25E-06	2.94E-06	3.83E-04	1.33E-05
liver	2.01E-04	0.20336	2.58E-02	1.47E-02	9.50E-03	6.22E-02
LK	6.89E-06	2.50E-03	0.12682	3.87E-3	1.11E-03	3.32E-04
RK	4.68E-06	1.54E-03	4.21E-03	0.12934	1.23E-03	8.26E-04
Skin	1.8E-01	3.73E-01	4.49E-01	4.56E-01	0.42178	1.78E-01
Tumor	3.13E-04	1.09E-02	6.04E-03	1.37E-02	8.04E-03	0.25303
Bone	1.43E-01	3.61E-02	3.21E-02	2.40E-02	3.60E-02	1.34E-02

Similar beta minus and positron results were observed in Patient 2.

Variations to the *F8 tally and the MODE card were tested but did not alter the positron and beta minus results. Further tests were run to assess the amount of energy that positrons and beta minus particles may deposit outside of the source tissue. A simple sphere surrounded with an *F8 tally was used as the representative source organ with the same composition and density used in the patient models. The dose contribution was found to be minimal outside of the source organ for both particles, and would not account for the observed differences. Further evaluation needs to take place to investigate the apparent model inconsistencies.

Using the average energies reported by the NNDC for the positrons and beta minus particles emitted by ^{65}Cu, Tables 7 and 8 show the expected absorbed fractions for Patient 1 and Patient 2.

Table 7: Predicted absorbed fractions for Patient 1 in Gy per decay of ^{64}Cu

Patient 1	Source						
Target	Brain	Liver	LK	RK	Skin	Tumor	Total
Brain	4.45E-16	5.49E-20	3.74E-22	3.49E-22	1.10E-18	3.98E-21	4.46E-16
Liver	5.41E-22	4.28E-15	6.09E-20	3.38E-20	2.45E-18	5.96E-20	4.29E-15
LK	2.46E-22	8.06E-18	7.17E-16	9.40E-20	2.91E-18	4.33E-20	7.28E-16
RK	1.11E-22	2.37E-18	9.75E-20	6.28E-16	2.98E-18	7.61E-20	6.34E-16
RT	5.42E-21	1.24E-18	2.27E-20	2.20E-20	1.43E-16	3.66E-20	1.45E-16
Tumor	4.99E-22	1.03E-18	9.58E-21	1.91E-20	1.18E-18	1.34E-16	1.36E-16
Bone	1.59E-19	4.18E-18	5.52E-20	4.00E-20	7.00E-18	9.50E-20	1.15E-17
						Whole Body	6.39E-15

Table 8: Predicted absorbed fractions for Patient 2 in Gy per decay of ^{64}Cu

Patient 2	Source						
Target	Brain	Liver	LK	RK	Skin	Tumor	Total
Brain	1.34E-15	1.30E-20	2.88E-24	1.04E-22	1.25E-18	1.63E-20	1.34E-15
Liver	2.99E-22	8.61E-15	8.13E-20	4.19E-20	1.87E-18	7.24E-21	8.61E-15
LK	8.46E-23	3.34E-18	3.33E-15	7.75E-20	1.99E-18	5.25E-21	3.33E-15
RK	1.07E-22	1.04E-18	5.71E-20	3.51E-15	2.01E-18	1.94E-21	3.51E-15
RT	1.03E-20	1.08E-18	3.06E-20	4.52E-20	3.17E-16	3.02E-20	3.18E-16
Tumor	6.09E-21	1.77E-19	1.58E-21	1.72E-21	1.35E-18	6.27E-16	6.29E-16
Bone	1.77E-19	2.12E-18	4.71E-20	5.94E-20	4.96E-18	1.07E-19	7.46E-18
						Whole Body	1.78E-14

The absorbed fractions in Tables 7 and 8 are hypothetical and assume that the energy of the emitted positrons and beta minus particles is deposited only within the source tissue. Additionally, dose contributions from the annihilation photons are not included into these estimates.

This internal dosimetric assessment only accounted for the radiation dose form a static distribution of ^{64}Cu-ATSM, and did not account for biological factors including redistribution

and excretion of the radiopharmaceutical. The presented results only estimates what the radiation dose would be from the decay of all administered radionuclides held at a constant spatial distribution. The biological factors that were excluded from these models are pivotal in the proper assessment of the internal radiation dose. The presented models provide a conservative estimate of radiation dose, but do not account for the redistribution of the radiopharmaceutical that is likely to occur, and would alter the percent distribution within the patient. Further assessment of the biokinetic behavior of ^{64}Cu-ATSM in both normal and cancer bearing canines will allow for improved dose assessments.

Conclusions

In an ongoing research effort to evaluate the clinical application of ^{64}Cu-ATSM as a cancer imaging agent selective for hypoxic environments, internal dosimetry of two cancer bearing canines patients treated with ^{64}Cu-ATSM was retrospectively conducted. Due to anatomical, breed, and malignancy variances between the two patients that could alter the internal distribution of ^{64}Cu-ATSM, patient specific voxel phantoms were created from the patient's PET/CT images that were compatible with Monte Carlo N Particle extended (MCNPX) radiation transport code. ^{64}Cu has the ability to emit both positrons and Auger electrons providing its possible application as a theranostic agent; therefore specific, absorbed fractions for the decay of ^{64}Cu were determined to provide a dynamic approximation of the relative radiation dose each patient would receive to their tumor and normal tissue if the administered activity of ^{64}Cu-ATSM was altered for further therapeutic purposes. These models are relative to the specific patient but can provide estimates for doses canine patients would receive in future trials.

References

Able Software Corp. (2015). 3D-Doctor User's Manual. Lexington, MA, USA. Retrieved from Able Software Corp.

Adams, S., Baum, R. P., Stuckensen, T., Bitter, K., & Hor, G. (1998). Prospective comparison of 18F-FDG PET with conventional imaging modalities (CT, MRI, US) in lymph node staging of head and neck cancer. *European Journal of Nuclear Medicine, 25*(9), 1255-1260.

Aerts, A., Impens, N. R., Gijs, M., D'Huyvetter, M., Vanmarcke, H., Ponsard, B., . . . Baatout, S. (2014). Biological Carrier Moleculed of Radiopharmaceuticals for Molecualr Cancer Imaging and Targeted Cancer Therapy. *Current Pharmaceutical Design, 20*(32), 5218-5244.

Avila-Rodriguez, M. A., Nye, J. A., & Nickles, R. J. (2007). Simultaneous production of high specific activity 64Cu and 61Co with 11.4 MeV protons on enriched 64Ni nuclei. *Applied Radiation and Isotopes, 65*(10), 1115-11120.

Bertout, J. A., Patel, S. A., & Simon, M. C. (2008). The impact of O2 Avalibility on Human Cancer. *Nature Reviews Cancer, 8*, 967-975.

Beyer, T., Townsend, D. W., Brun, T., Kinahan, P. E., Charron, M., Roddy, R., . . . Nutt, R. (2000). A Combined PET/CT Scanner for Clinical Oncology. *The Jornal of Nuclear Medicine, 41*(8), 1369-1379.

Boellaard, R., O'Doherty, M. J., Weber, W. A., Mottaghy, F. M., Stroobants, S. G., Oyen, W. J., . . . Comans, E. F. (2010). FDG PET and PET/CT: EANM procedure guidelines for tumor PET imaging: version 1.0. *European Journl of Nuclear Medicince and Molecular Imagine, 37*, 181-200.

Bolch, W. E. (2002). *Practical Applications of Internal Dosimetry* . Madison, WI: Medical Physics Publishing .

Bushberg, J. T., Seibert, J. A., Leidholdt, E. M., & Boone, J. M. (2012). *The Essential Physics of Medicl Imaging.* Philadelphia, PA: Lippicott Williams & Wilkins.

Caffrey, E. (2013). Craetion of a Voxel Phantom of the ICRP Reference Crab. *Journal of Environmental Radioactivity , 120*, 14-18.

Carreau, A., El Hafny-Rahbi, B., Matejuk, A., Grillon, C., & Kieda, C. (2011). Why is the Partial Oxygen Presure of human tissues a crucial parameter? Small Molecules and Hypoxia. *Journal of Cell and Molecular Medicine, 15*(6), 1239-1253.

Cember, H., & Johnson, T. E. (2009). *Introduction to Health Physics.* The McGraw-Hill Companies.

Dearling, J. L., Lewis, J. S., Mullen, G. E., Welch, M. J., & Blower, P. J. (2002). Copper bis(thiosemicarbazone) complexes as hypoxia imaging agents: structure-activity relationships. *Journal of Biological Inorganic Chemistry, 7*(3), 249-259.

Eckerman, K. F., Westfall, R. J., Ryman, J. C., & Cristy, M. (1994). Availability of nuclear decay data in electronic form, including beta spectra not previously published. *Health Physics, 67*(4), 338-345.

Fujibayashi, Y., Taniuchi, H., Yonekura, Y., Ohtan, i. H., Konishi, J., & Yokoyama, A. (1997). Copper-62-ATSM: a new hypoxia imaging agent with high membrane permeability and low redox potential. *Journal of Nuclear Medicine, 38*(7), 1155-1160.

Fukuda, Y., & Collaboration, S.-K. (1998). Evidence for Oscillation of Atmospheric Neutrinos. *Physical Review Letters, 81*(8).

Gambhir, S. S. (2002). Molecular imaging of cancer with positron emission tomography. *Nature Reviews Cancer*, 683-693.

Gingras, B. A., Suprunchuk, T., & Bayley, C. H. (1961). The Preperation of some Thiosemicarbazones and Their copper Complexes. *Journal of Chemistry, 39*(5), 973-985.

Hall, E. J. (2012). *Radiobiology for the Radiologist.* Philadelphia, PA: Lippincott Williams & Wilkins .

Hess, S., Blomberg, B. A., Zhu, H. J., Høilund-Carlsen, P. F., & Alavi, A. (2014). The Pivotal Role of FDG-PET/CT in Modern Medicine. *Academic Radiology, 21*(2), 232-249.

ICRP. (1959). *Permissible dose for Internal Radiation.* Pergamon Press.

ICRP. (1975). *Report on the Task Group on Reference Man.* ICRP Publication 23.

ICRP. (1979). *Limits for Intake of Radionuclides by Workers.* ICRP Publication 30.

Kalos, M. H., & Whitlock, P. A. (2008). *Monte Carlo Methods* . Livermore , USA: Wiley-VCH Verlag GmbH & Co.

Kramer, G. H. (2010). Tools for Creating and Manipulating Voxel Phantoms. *Health Physics, 98*(3), 542-548.

Martinelli, L. D., & al., e. (1949). Dosage Determination in the use of Radioactive Isotopes. *The Journal of Clinical Investigation, 28*(6), 1271-1280.

Martinez, N. E., Johnson, T. E., Capello, K., & Pinder, J. E. (2014). Development and comparison of computational models for estimation of absorbed organ radiation dose in rainbow trout (Oncorhynchus mykiss) from uptake of iodine-131. *Journal of Environmental Radioactivity, 138*, 50-59.

Maurer, R. I., Blower, P. J., Dilworth, J. R., Reynolds, C. A., Zheng, Y., & Mullen, G. E. (2002). Studies on the Mechanism of Hypoxic Selectivity in Copper Bis(Thiosemicarbazone) Radiopharmaceuticals. *Journal of Medical Chemistry, 45*(7), 1420-1431.

McConn, R. J. (2010). *Compendium of Material Composition Data for Radiation Transport Modeling.* Pacific Northwest National Labortatory . Oak Ridge : United States Department of Homeland Security .

McMillan, D. D. (2015). Validation of 64-Cu-ATSM damaging DNA via high-LET Auger electron emission. *Journal of Radiation Research, 56*(5), 784-791.

McMillian, D. D. (2013). Evaluation of Cu-64-ATSM in Cell Culture for Potential Use As a Radiotherapy Agent. *(Masters Thesis).*

McParland, B. J. (2010). *Nuclear Medicine Radiation Dosimetry Advanced Theoretical Principles.* London: Springer-Verlag.

NNDC. (2015). *Chart of Nuclides*. Retrieved from National Nuclear Data Center: http://www.nndc.bnl.gov/chart/

Philips Clinical Informatics . (2015). Retrieved from Intellispace Portal 7.0: http://www.usa.philips.com/healthcare/education-resources/resource-library

Ruedig, E., Beresford, N. A., Gomez Fernandez, M. E., & Higley, K. (2015). A comparison of the ellipsoid and voxelized dosimetric methodologies for internal, heterogeneous radionuclide sources. *Journal of Environmental Radioactivity, 140*, 70-77.

SNMMI. (2015). Committee on Medical Internal Radiation Dose (MIRD). Reston, Va, USA.

Snyder, S. W., & al, e. (1978). *Estimates of Specific Absorbed Fractions for Photon Sources Uniformly Distributed in Various Organs of a Heterogeneous Phantum* . New York : Society of Nuclear Medicine; Medical Internal Radiation Dose Committee.

Snyder, W. e. (1975). *Absorbed dose per unit cumulated activity for select radionuclides and organs. MIRD Pamphlet No. 11.* New Your : Society of Nuclear Medicine .

Strauss, L. G., & DimitrakopoulouStrauss, A. (2008). The role of PET in head and neck cancer. *Hellenic Journal of Nuclear Medicince, 11*(1), 6-11.

The Radiation Dose Assessment Resource . (n.d.). *Welcome to RADAR*. Retrieved 2015, from RADAR : http://www.doseinfo-radar.com/RADARHome.html

Turner, J. E. (2008). *Atoms, radiation, and radiation protection.* John Wiley & Sons.

Weinberg, R. A. (2007). *the Biology of Cancer.* New York : Garland Science, Taylor & Francis Group .

Xu, X. G., & Eckerman, K. F. (2009). *Handbook of Anatomical Models for Radiation Dosimetry.* Boca Raton, FL: Taylor & Francis Group.

Xu, X. G., Chao, T. C., & Bozukurt, A. (2000). VIP-MAN: An Image-Based Whole-Body Adult Male Model Constructed from Color Photographs of The Visable Human Project for Multi-Particle Monte Carlo Calculations. *Health Physics, 78*(5), 476-486.

Zaidi, H., & Sgouros, G. (2003). *Therapeutic Applications of Monte Carlo Calculations in Nuclear Medicine.* Bristol: Institute of Physics Publishing.